

Local Impact of Pt Nanodeposits on Ionomer Decomposition in Polymer Electrolyte Membranes

S. Helmly¹ · M. J. Eslamibidgoli² · K. A. Friedrich^{1,3} · M. H. Eikerling²

Published online: 2 February 2017

© The Author(s) 2017. This article is published with open access at Springerlink.com

Abstract Based on recent theoretical studies, we designed a multistep experimental protocol to understand the impact of environmental conditions around Pt nanodeposits on membrane chemical degradation. The first experiment probes the local potential at a Pt microelectrode for different rates of permeation of hydrogen and oxygen gases from anode and cathode side. The subsequent degradation experiment utilizes the local conditions taken from the first experiment to analyze local rates of ionomer degradation. The rate of ionomer decomposition is significantly enhanced in the anodic H₂-rich membrane region, which can be explained with the markedly increased amount of H₂O₂ formation at Pt nanodeposits in this region.

Keywords Ionomer decomposition · Pt in the membrane · Hydrogen peroxide formation · Local reaction conditions

Introduction

The viability of polymer electrolyte fuel cell (PEFC) technology for transportation applications is critically dependent on the durability of the polymer electrolyte membranes (PEM). The PEM fulfills key functions in PEFCs as electronic

insulator, gas-separating medium, and proton conductor [1]. Understanding the PEM degradation problem is particularly important for next-generation heavy duty fuel cell stacks for buses that demand an operational lifetime of at least 20,000 h [2].

The chemical degradation of PEM is accelerated by conditions such as low relative humidity (RH), high temperature, and high cell voltage [3–5]. The problem is aggravated by the excessive thermal and humidity cycling as seen in accelerated degradation tests [6]. Chemical degradation of PEM causes a decrease of the ionomer molecular weight, a loss of ion exchange capacity, and membrane thinning [7]. These structural changes result in measurable changes of the proton conductivity, and they facilitate membrane failure triggered by the formation of pinholes and cracks [8–10].

Deposits of Pt in the membrane (PITM), which originate from Pt dissolution in the cathode catalyst layer [11], play an important role in membrane chemical degradation. Chemical degradation is linked to the attack of the weak bonds in ionomer side chains by radical species. The main type of radical species, hydroxyl radicals, is formed by the reaction of hydrogen peroxide, H₂O₂, at impurities such as Fe²⁺ [12, 13], which are present in small amounts due to the dissolution of end plates in contact with humidified oxygen and hydrogen [14–16]. H₂O₂—the main chemical compound responsible for chemical PEM degradation—is the product of surface reactions of H₂ and O₂ at PITM [17–23].

The net rate of H₂O₂ formation at PITM depends on the size, shape, and distribution of Pt nanoparticles in the membrane and local reaction conditions around particles, determined by temperature, electrical potential, reactant concentrations, pH, and RH [12–18, 24–31].

The permeation of reactant gases leads to concentration profiles of H₂ and O₂ that determine the distribution of the

✉ M. H. Eikerling
meikerl@sfi.ca

¹ Institute of Engineering Thermodynamics, German Aerospace Center, Pfaffenwaldring 38–40, 70569 Stuttgart, Germany

² Department of Chemistry, Simon Fraser University, 8888 University Drive, Burnaby, BC V5A 1S6, Canada

³ Institute of Energy Storage, University of Stuttgart, Pfaffenwaldring 31, 70569 Stuttgart, Germany

electrical potential in the PEM, essentially forming two distinct potential regions [32]. In the anodic region, with a high ratio of H_2 to O_2 concentration, the electrical potential is close to the equilibrium potential of the hydrogen oxidation reaction (HOR). In the cathodic region, with a high ratio of O_2 to H_2 concentration, the electrical potential settles in the potential range of 0.8 V vs. reversible hydrogen electrode (RHE). The width of anodic and cathodic regions depends on the ratio of partial pressures of H_2 and O_2 at the PEM boundaries as well as the gas diffusivities in the membrane [32].

It was seen that the chemical PEM degradation, indicated by the fluoride emission rate (FER), was higher when particles were of cubic shape [27]. In contrast, irregular structures such as tree-like, curly dendritic, and star-shaped particles exhibited lower FER [27]. The authors in [27] assumed that the larger surface area fraction of Pt(111) facets of the structured particles leads to a higher catalytic activity toward peroxide quenching [27]. Regarding the particle distribution, it was reported that chemical degradation was lower when particles were densely distributed [26, 31]. Furthermore, it was observed that Pt in the anodic region causes higher peroxide formation and higher FER than Pt in the cathodic region [18, 19, 31].

Different electrochemical conditions around PITM influence the reaction pathway of oxygen reduction at Pt deposits. Experimental studies [34–39], as well as a recent density functional theory (DFT) investigation [33], revealed that the formation of H_2O_2 is enhanced at hydrogen-covered Pt surface that is expected to occur in the anodic region of the PEM.

In the past, the effects of Pt particle shape, particle density, and local reaction conditions around nanodeposits have been studied in separation only and not concurrently. In most studies, the extent of work did not allow to control and vary all three conditions simultaneously. Therefore, they poorly reflect the processes that occur under real operation. For example, on the one hand, studies exploring the impact of the PITM distribution did not take into account the influence of the electrochemical environment [20, 26, 30, 31]. On the other hand, studies of the electrochemical environment did not consider the impact of the PITM distribution [18, 19]. However, due to the reported correlated effects of all three conditions, it is necessary to control them simultaneously to obtain complete and representative results.

This paper presents results of a two-step validation experiment that corresponds to a stepwise theoretical approach presented in refs. [32, 33]. The combined experimental-theoretical approach is displayed in Fig. 1. In brief, in the first step, the local electrostatic potential at Pt deposits in the membrane was calculated using a continuum model of reactant crossover in the membrane coupled with local electrochemical reactions at Pt deposits [32]. Given the local potential obtained from this model, the surface adsorption state of Pt was identified, using pertinent experimental data. Thereafter, DFT calculations were performed for a model system of a Pt(111)-

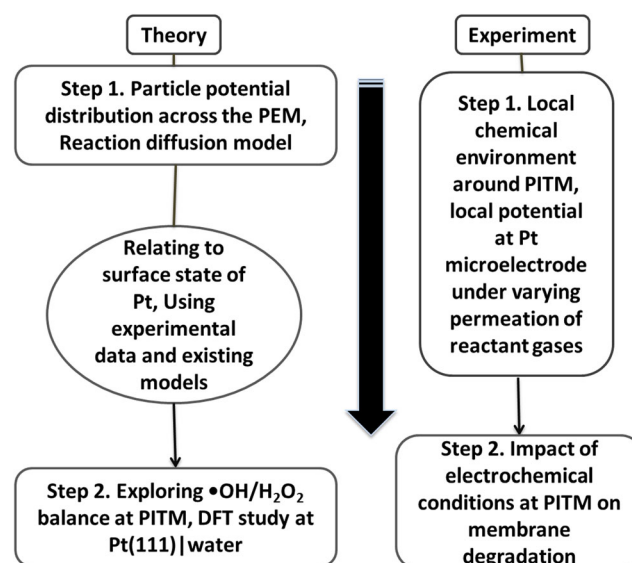


Fig. 1 Approach to investigate the role of electrochemical conditions around Pt nanodeposits in the membrane on ionomer decomposition

water interface to study the oxygen reduction reaction (ORR) in view of the propensity for the formation of hydrogen peroxide. These DFT studies were performed at three surface adsorption states of Pt that corresponded to the local electrode potentials identified in the continuum model [33]. It was found that in the low potential region, the rate of the $2 e^-$ reduction of O_2 to H_2O_2 is strongly enhanced due to kinetic inhibition of the $4 e^-$ ORR [34].

Consequently, this paper focuses on the impact of electrochemical conditions at PITM, distributed as a band consisting of cubic particles, on chemical degradation in PEMs. Following the logics of theoretical studies, the first experiment serves to determine the local electrical potential at PITM as a function of H_2 and O_2 concentrations at the PEM boundaries. For this purpose, a PEM was prepared with a Pt microelectrode embedded into it and the external reactant concentrations were varied. In the second step, a PEM with a narrow band of PITM was held under specific electrochemical conditions to maintain either anodic or cathodic reaction conditions at the position of the Pt band. In this configuration, the FER was measured to quantify the extent of PEM degradation.

Experimental Details

A multilayer PEM with an embedded Pt microelectrode was prepared according to the method described in refs. [16, 40, 41]. Six membranes were stacked in series to form a multimembrane unit (MMU) with a nominal thickness of 200 μm . The Pt wire electrode of 40 μm diameter was placed between the two central membranes. For sensing the Pt potential, each end of the Pt wire was soldered to an isolated copper wire which protruded from the electrolyte. Subsequently, the

MMU together with the Pt microelectrode were hot pressed as described below. The general configuration of this cell is shown in Fig. 2. The usage of several membranes was necessary to increase the ratio between the electrolyte thickness and the diameter of the Pt wire in order to achieve a sufficient spatial resolution for potential sensing.

The membranes used were chemically stabilized Nafion® NRE-211CS (25 μm thick, DuPont) and NRE-212CS (50 μm thick, DuPont), with a size of 65×65 mm. The duplicate contacting of the wire not only yielded a backup contact for potential sensing but also allowed checking for contact problems such as breaking of the mechanically weak Pt wire.

The electrode attached on the anode side of the membrane served as both counter and reversible hydrogen electrode. The membrane was coated beforehand with a catalyst layer at an area of 25 cm^2 by dry spraying [42] and hot pressed with a supporting gas diffusion layer (Sigracet GDL 25 BC, SGL Technologies GmbH) for 5 min at $160 \text{ }^\circ\text{C}$ with 700 N cm^{-2} . The catalyst layer consisted of Pt black (HiSPEC 1000, Johnson Matthey Fuel Cells) and 30 wt% Nafion® ionomer powder. The ionomer powder used in the dry spraying technique is produced by freeze milling Nafion® resin NR-50 (DuPont). The Pt loading was $0.3 \text{ mg}_{\text{Pt}} \text{ cm}^{-2}$. Lastly, the MMU with the microelectrode was hot pressed for 5 min at $180 \text{ }^\circ\text{C}$ with 700 N cm^{-2} .

For operating this cell, it was equipped with an additional gas diffusion layer (Sigracet SGL-BC25) on the oxygen side and gaskets (Freudenberg FC-PO, $350 \mu\text{m}$ thick) on both sides. This assembly was sandwiched between two cell holders, which were bolted together with a tightening torque of 3 Nm. The flow field in the cell holders had a single serpentine channel. Both cell holders were arranged in co-flow configuration. The cell was operated in a test station at $80 \text{ }^\circ\text{C}$. For gas humidification, humidifiers were used which allowed the control of the humidity level by adjusting the dew point temperature. The dew point temperature was set to $76 \text{ }^\circ\text{C}$. H_2 and O_2/air were fed to the cell, each with a flow rate of 100 sccm. The concentration of H_2 and O_2 at the Pt microelectrode was varied by controlling the reactant pressure at the inlet of the cell holder. The electrical potential of the Pt microelectrode vs. RHE was measured with the potentiostat IM6 (Zahner Elektrik).

The degradation experiment was performed with four cells containing an MMU but differing regarding the presence of PITM and catalyst layers. The four configurations were MMU without PITM, MMU with PITM, catalyst-coated MMU (CCM) without PITM, and CCM with PITM (see Fig. 3). In cells without PITM, pristine membranes were used whereas in cells with PITM, the central membrane of the MMU contained PITM, which was deposited beforehand in a process described in the next section. The optional catalyst layers were prepared with Pt black as described above. This catalyst was selected due to the relatively large crystallite size of its Pt particles of around 9 nm,

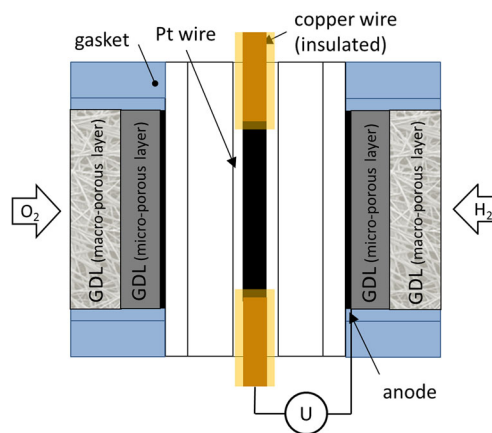


Fig. 2 Cell configuration of Pt microelectrode placed in a multimembrane unit

which improves its thermodynamic stability. Therefore, additional Pt deposition from the catalyst layers during operation was avoided [31]. The MMU was hot pressed with gas diffusion layers (GDL) on both sides (Sigracet GDL 25 BC, SGL Technologies GmbH) for 5 min at $160 \text{ }^\circ\text{C}$ with 700 N cm^{-2} .

For operation in the test station, the cells were mounted in the test station as single cells via cell holders as described above. In the degradation test, the cells were operated at different settings of reactant pressures, which yielded either a low or high potential of the PITM. The settings were chosen based on the results from experiment with the Pt microelectrode and kept for 24 to 70 h each. To check for reproducibility, the settings were repeated. The cell temperature was set to $80 \text{ }^\circ\text{C}$. H_2 and O_2 were fed to the cells with equal flow rates of 40 sccm at $76 \text{ }^\circ\text{C}$. The cells were not electrically connected, which means that current or voltage was not controlled. During the degradation test, condensate water from anode and cathode side was collected in polyethylene bottles for analysis of fluoride emission.

For obtaining a blank, i.e., uncoated, membrane containing typical Pt precipitations, Pt was deposited from the catalyst of

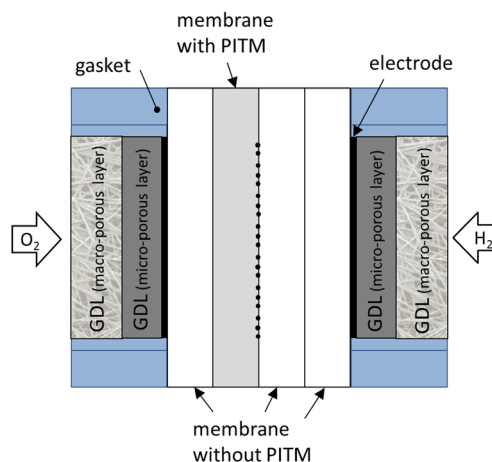


Fig. 3 Cell configuration for membrane degradation tests

a single-side catalyst coated membrane (geometric electrode area: 5×5 cm, IP111, Ion Power, Inc.) into a blank Nafion[®] membrane (size: 6.5×6.5 cm, NRE-212CS, DuPont) under fuel cell operating conditions. For this, the membranes were arranged to each other so that the catalyst layer of the IP111 was facing the blank membrane. In order to increase O₂ transport across the IP111 membrane to the catalyst layer, the catalyst-coated membrane was perforated with a scalpel beforehand. The combined membranes were sandwiched between GDL, which was the Sigracet GDL 25 BC (SGL Technologies GmbH) on the side of the IP111 and a Sigracet GDL 25 BA (SGL Technologies GmbH) on the side of the NRE-212CS. The latter GDL was used because it did not include a microporous layer. Thereby, the contamination of the membrane by deposition of carbon from the MPL was avoided. The arrangement of the membranes is shown in Fig. 4. This cell was then assembled in the same way as described above and operated in the test station for 64 h at OCV. As in the other experiments, the cell temperature was set to 80 °C and the temperatures of the humidifiers to 76 °C. For dissolving the Pt in the catalyst layer, 50 sccm O₂ was supplied at 150 kPa to the side of the catalyst-coated membrane. The Pt ions in the blank membrane were reduced to metallic Pt by feeding 50 sccm H₂ with 110 kPa to the membrane. After the preparation of the PITM membrane, the NRE-212CS membrane (containing now PITM) was separated from the CCM and rinsed for 4 h in demineralized water which was heated to 60 °C and stirred in a beaker with a speed of 500 rpm. After drying the membrane between precision wipes (Kimtech, Kimberly-Clark), it was ready for usage as the PITM membrane in a MMU for the degradation experiment.

Membrane decomposition was measured based on fluoride ion concentration, c_{F^-} [$\mu\text{mol}_{F^-} \text{ l}^{-1}$], in the collected condensate (with mass m [kg]). The concentration was measured with an ion-selective electrode (laboratory meter ProLab 4000 and fluoride electrode F 60, SCHOTT Instruments). The electrode was calibrated over the range of 10–10,000 $\mu\text{mol}_{F^-} \text{ l}^{-1}$ using KF aqueous standard solutions. The standard samples and condensate samples (15 ml) were diluted with buffer solution (TISAB II, Bernd Kraft GmbH) with a ratio of 1:1. The reading of the meter was recorded after equilibrium was reached: typically 5–10 min after the electrode was immersed into the solution. The error of the given measurement data includes the electrode error of $\pm 2\%$ and the error of the laboratory meter of ± 0.1 mV. Based on c_{F^-} , and taking into account the geometric electrode or GDL area, A [m^2], the density of water, $\delta = 0.997$ [kg m^3], and the duration of collecting the condensate, t [h], the fluoride emission rate (FER) was calculated as $\text{FER} = (c_{F^-} \times m) / (A \times \delta_{\text{H}_2\text{O}} \times t)$ [$\mu\text{mol}_{F^-} \text{ cm}^{-2} \text{ h}^{-1}$].

The membrane cross sections were examined with SEM to determine the position of the PITM and the distribution of Pt particles (Table 1). Samples with a width (i.e., cross-sectional length) of approximately 3 mm were cut from the CCM and

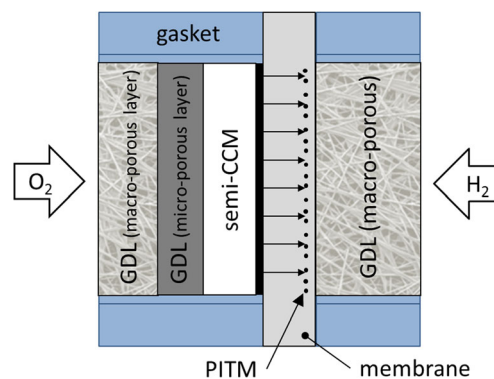


Fig. 4 Cell configuration for Pt deposition in the membrane

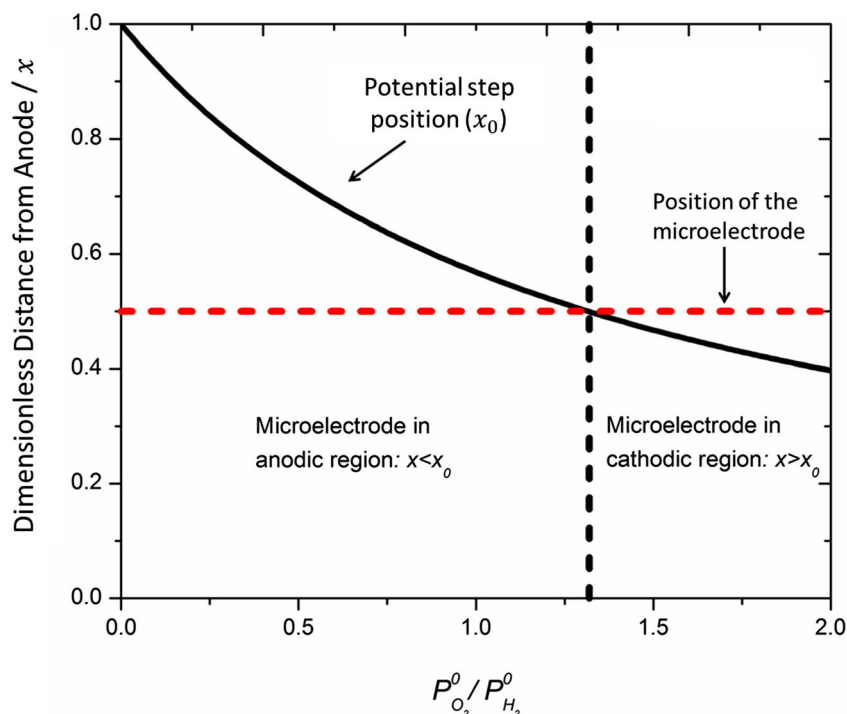
MMU with PITM after operation in the test station. For preparation of cross sections via freeze fractioning, GDLs were removed from the samples, which were then immersed in liquid nitrogen and broken. SEM measurements were conducted on an ULTRA plus (Zeiss Corp.) scanning electron microscope. The images were recorded based on secondary electrons (SE) and backscattered electrons (BE) at 3 or 5 kV. The resolution of the SEM was 1.0 nm at 15 kV and 1.7 nm at 1 kV. SEM micrographs were analyzed with the ImageJ 1.46r software (National Institutes of Health) to determine the number of single Pt particles as well as their position and area. Based on these data, the equivalent particle diameter and the nearest neighbor distance were calculated for each particle. For each membrane electrode assembly (MEA) sample, the single values of diameter and distance were averaged. Furthermore, the particle density, i.e., the ratio of the image area covered by particles to the total image area, and the particle intensity, i.e., the number of particles in the total image area, were determined.

Results and Discussion

Dependence Between Reactant Concentration Ratio and Electrical Potential at PITM

As discussed in ref. [32], the local mixed potential at a Pt nanoparticle, considered as a nanoelectrode in the PEM, is caused by both the HOR and the ORR proceeding simultaneously at the particle surface. For a Pt nanodeposit at position x from the anode side in the PEM, if the limiting current density of the HOR is greater than that for the ORR, the HOR is controlled by reaction kinetics and the ORR is diffusion limited; in this case, the mixed potential remains close to the equilibrium potential of the HOR. On the other hand, if the limiting current density of the HOR is smaller than that for the ORR, then the HOR is diffusion limited and the ORR is kinetically controlled; in this case, the mixed potential is shifted toward the equilibrium potential of the ORR. The transition between the two cases occurs at the position where limiting current densities of HOR and ORR are equal; in

Fig. 5 Potential step position in the membrane as a function of relative partial pressure of O₂ and H₂. For a microelectrode at $x = 0.5$, shown as a horizontal dashed line, pressure ratio smaller than ~ 1.3 leaves it in the anodic region, while pressure ratio larger than ~ 1.3 leaves it in the cathodic condition. The distinction between the two regions is shown as a vertical dashed line



this case, the current density at the particle is independent of potential. This corresponds to a step-like change in potential profile at a position, x_0 , which can be obtained as [32]

$$x_0 = \frac{l}{1 + 2\beta \frac{P_{O_2}^0}{P_{H_2}^0}}, \quad (1)$$

where $\beta = \frac{D_{O_2}H_{O_2}}{D_{H_2}H_{H_2}}$ is experimentally reported as 0.38 ± 0.05 at 100% RH and 65 °C [29]; l is the membrane thickness; $P_{H_2}^0$ and $P_{O_2}^0$ are the partial pressures of hydrogen and oxygen at anode |

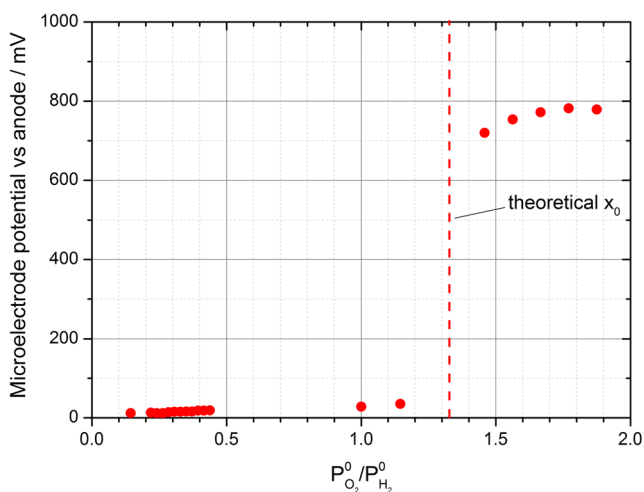


Fig. 6 Experimental measurement of mixed potential at microelectrode caused by permeation of H₂ and O₂ in the membrane as a function of relative pressures at the membrane boundaries. Results are in agreement with the model prediction shown in Fig. 5

membrane and cathode | membrane boundaries, respectively; D_{H_2} and D_{O_2} are the diffusion coefficients of hydrogen and oxygen in the membrane, respectively; and H_{H_2} and H_{O_2} are the corresponding Henry's law constants.

In Fig. 5, x_0 is shown as a function of the relative pressure of oxygen and hydrogen at the membrane boundaries. As discussed, at the step position, the PEM is divided into a low potential region (between the anode and the step) and a high potential region (between the step and the cathode). When the microelectrode is positioned at $x = 0.5$, as it is the case in our experiment, for $P_{O_2}^0/P_{H_2}^0 < 1.3$, it should be exposed to anodic conditions with a potential close to the equilibrium potential of the HOR. In contrast, at higher pressure ratios, cathodic conditions should be induced resulting in a potential value that lies in the range of 0.8 V vs. RHE. Therefore, from Eq. (1), the local reaction condition around Pt nanodeposits in the membrane, determined by various pressure settings, can be linked to the local potential of Pt nanoparticles.

The experimental data from our first experiment agrees well with this calculation of the potential step. As can be seen in Fig. 6, the change between low potential and high potential conditions at the microelectrode is clearly visible as $P_{O_2}^0/P_{H_2}^0$ changes from 1.15 to 1.46. This observed step-like change in electrical potential is also in good agreement with other studies [16, 40] as described in ref. [32] Based on the gained data, the following pressure settings are selected to locally obtain either low potential or high potential conditions at PITM in the second experiment, which is described in the next section: $P_{O_2}^0/P_{H_2}^0 = 0.69$ for anodic conditions and $P_{O_2}^0/P_{H_2}^0 = 1.46$ for cathodic conditions.

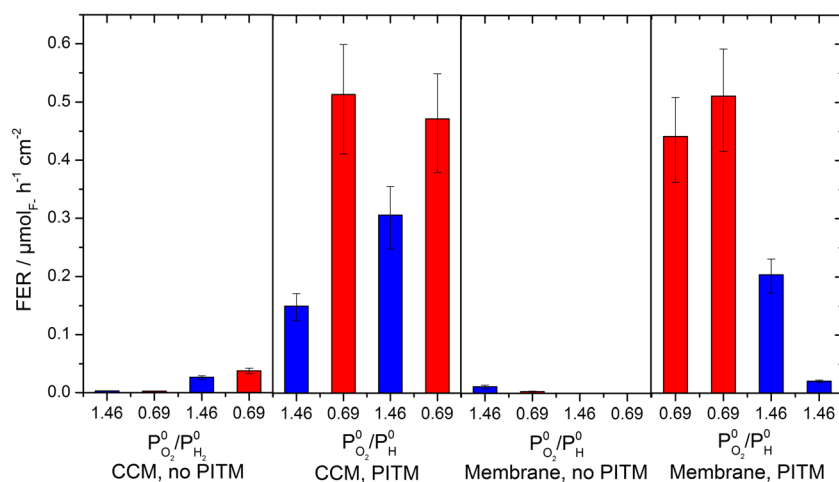


Fig. 7 FER measurement for various cell configurations at the two pressure settings $P_{\text{O}_2}^0/P_{\text{H}_2}^0 = 0.69$ (red) and $P_{\text{O}_2}^0/P_{\text{H}_2}^0 = 1.46$ (blue) indicating higher ionomer decomposition if PITM is present in the low potential region (i.e., $P_{\text{O}_2}^0/P_{\text{H}_2}^0 = 0.69$)

Impact of Electrochemical Conditions at PITM on Membrane Degradation

Degradation tests were performed for cells of different configurations (with/without PITM, with/without electrodes), under the two pressure settings mentioned above. The FER data in Fig. 7 show that polymer decomposition is higher for PITM present under anodic conditions ($P_{\text{O}_2}^0/P_{\text{H}_2}^0 = 0.69$) as compared to PITM present under cathodic conditions ($P_{\text{O}_2}^0/P_{\text{H}_2}^0 = 1.46$). This observation is consistent with the expectation of a higher rate of H_2O_2 formation at Pt nanodeposits that are held under anodic conditions, viz. in the H_2 -rich membrane region. Besides, our results obtained with a realistic PITM density and distribution case agree with studies in which the PITM distribution was not controlled [18, 19].

Moreover, it can be noted that the FER values exhibited a stronger variation at cathodic conditions than at anodic conditions, especially for the membranes that contained PITM. The example of CCM with PITM shows that the FER values changed by 51% at cathodic conditions but only by 8% at anodic

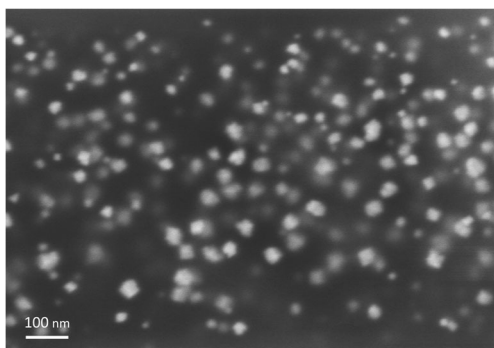


Fig. 8 Scanning electron microscope (SEM) image of Pt nanodeposits in the membrane

conditions. Obviously, the FER values at a given setting were influenced by the previous setting. Especially under cathodic conditions; it can be seen from the chronological order of settings in Fig. 7 that consecutive switching between anodic and cathodic settings, as in the case of the PITM CCM, led to convergence of the FER values of anodic and cathodic conditions to each other; whereas this effect was not observed when repeating the same setting, as in the case of the PITM membrane. To give an example, the FER value obtained at cathodic conditions was increased by an intermittent switch to anodic conditions, while a repetition of the cathodic setting caused a decrease of the FER value. A possible explanation for this could be the relatively slow removal of polymer fragments from the membrane due to the relatively high membrane thickness (200 μm). As a consequence of the slow transport, polymer fragments decomposed during a setting could have ended up in the condensate collected during the subsequent setting.

The effect that PITM increases membrane decomposition when formed as a typical Pt band during operation, as also proven in ref. [22], is confirmed by the observation that cells with PITM had a higher FER than the PITM-free cells. The controversy as to whether membrane degradation is increased or inhibited by PITM, as discussed in refs [19, 24–27], might be related to the influence of particle morphology and particle density. In ref. [27], an inhibiting effect on membrane degradation is observed, exerted by particles with a star or dendritic shape, which means particles with high proportion of Pt(111) surface facets. In contrast, inhibited degradation by Pt particles with cubic or spherical shape was not found. However, a correlation between degradation and PITM concentration as well as particle size is also indicated: the lowest degradation was observed for the membrane with the highest PITM concentration and the largest particles (~2 μm). As can be seen in the micrograph in Fig. 8, Pt particles in cells that were tested in our study had cubic shape and

were relatively small (~10 to 20 nm), which is consistent with the absence of an inhibiting effect of PITM.

In ref. [19], the authors observed that the FER depends on PITM concentration. The dependence is non-linear; the FER is highest at low PITM concentration and decreases with increasing PITM concentration with the result that at 50 mol% Pt, the FER was 15% lower compared to 0 mol% Pt. According to this finding, PEM chemical degradation is clearly inhibited by PITM. It should be mentioned that in this case, PITM was deposited *ex situ* and throughout the whole membrane. An even stronger inhibiting effect was reported by Aoki et al. (ca. 74% and 90% FER reduction with PITM membrane compared to a Pt-free H⁺ membrane [19]) and Endoh et al. (ca. 74% FER reduction with PITM MEA compared to a standard MEA [43]). In both studies, membranes were used, which contained uniformly dispersed PITM.

In our results, the influence of PITM was independent of the presence of electrodes as revealed by the comparative analysis of FER values seen in PITM cells with electrodes (CCM, PITM) and without electrodes (membrane, PITM). This observation is a clear indication that H₂O₂ involved in membrane degradation had been formed at PITM and not at electrodes. In this aspect, our results differ from the observation of increased degradation due to the presence of electrodes [22]. This disagreement can be explained by the different catalysts used in both experiments. Whereas carbon-supported Pt was used in the electrodes of Hasegawa et al. [22], unsupported Pt black was used in our electrodes. As reported in ref. [43], hydroxyl radical formation is significantly lower if electrodes contain Pt black instead of Pt/C.

Higher degradation at Pt nanodeposits in the low potential region can be explained by the dependence on the rate of H₂O₂ formation at Pt nanodeposits, which is enhanced in the anodic potential region, *viz.* at high cathodic overpotentials. The potential determines the Pt surface adsorption state, which affects the reaction pathway of the oxygen reduction [33]. Under anodic conditions, for Pt particles in the H₂-rich region of the PEM, the particle surface is covered with hydrogen; it is known that the 2 e⁻ reduction pathway of oxygen that leads to significant H₂O₂ formation is markedly enhanced in this potential regime, controlling the rate of radical-initiated chemical degradation [13].

Conclusions

In this article, a two-step experimental strategy is presented to explore the role of environmental conditions around PITM, distributed as a band consisting of cubic particles, on ionomer decomposition in PEMs. In previous studies on this topic, PITM had been distributed widely throughout the whole membrane and thus O₂-rich and H₂-rich conditions existed simultaneously. In the work presented in this article, defined electrochemical

conditions at PITM were ensured by depositing PITM locally and controlling the local electrochemical conditions. It was discussed that the step-like potential distribution at Pt nanodeposits divides the PEM into two regions, with low potential (~0 V) or high potential (~0.8 V). The position of the potential step is governed by the ratio of the partial pressure of reactant gases at the membrane boundaries as well as the permeability properties of the PEM. This was validated in the first step, where the partial pressures of H₂ and O₂ at the membrane boundaries were varied in order to induce anodic or cathodic reaction conditions at a Pt microelectrode embedded into the membrane. In the second step, the effect of various pressure settings (or local potential at PITM) on radical-initiated membrane degradation was explored by measuring the fluoride emission rate as the descriptor of ionomer decomposition. Consistent with DFT-based modeling of Pt surface reactions, it was demonstrated that PITM located in the low potential region of the membrane leads to significantly higher ionomer decomposition rate as compared to the case where PITM is located in the high potential region. This effect is due to significant H₂O₂ formation at hydrogen-covered Pt nanodeposits in the low potential region.

On the practical side, findings presented in this article open up possibilities to suppress ionomer decomposition in PEMs by smart control of fuel cell operating conditions. Operating protocols should be devised that minimize exposure of Pt deposits in the PEM to hydrogen-rich conditions, *i.e.*, hydrogen partial pressures should generally be kept low and lower than oxygen partial pressures. This could be particularly feasible during start-up and shut-down conditions.

Acknowledgements MJE and MHE acknowledge the financial support by an Automotive Partnership Canada grant project on “Next Generation Heavy Duty Fuel Cell Buses (APC-HDFC),” which was supported by Ballard Power Systems.

Appendix

Pt distribution

Table 1 Distribution of Pt particles in the Pt band

	Particle density (area specific)/%	Particle intensity 1/nm ²	Average particle diameter/nm	Average minimum particle distance/nm
CCM, PITM	10.9	0.00130	10.0 ± 2.8	17.8 ± 5.3
Membrane, PITM	13.1	0.00051	17.1 ± 5.8	33.0 ± 10.3

Data are based on micrographs. Distribution differed because of different experiment settings

Open Access This article is distributed under the terms of the Creative Commons Attribution 4.0 International License (<http://creativecommons.org/licenses/by/4.0/>), which permits unrestricted use, distribution, and reproduction in any medium, provided you give appropriate credit to the original author(s) and the source, provide a link to the Creative Commons license, and indicate if changes were made.

References

- M.P. Rodgers, L.J. Bonville, H.R. Kunz, D.K. Slattery, J.M. Fenton, *Chem. Rev.* **112**, 6075–6103 (2012)
- S.D. Knights, K.M. Colbow, J. St-Pierre, D.P. Wilkinson, *J. Power Sources* **127**, 127–134 (2004)
- T. Madden, D. Weiss, N. Cipollini, D. Condit, M. Gummalla, S. Burlatsky, V. Atrazhev, *J. Electrochem. Soc.* **156**, B657–B662 (2009)
- F. De Bruijn, V. Dam, G. Janssen, *Fuel Cells* **8**, 3–22 (2008)
- J. Wu, X. Zi Yuan, J.J. Martin, H. Wang, J. Zhang, J. Shen, S. Wu, W. Merida, *J. Power Sources* **184**, 104–119 (2008)
- T. Jahnke, G. Futter, A. Latz, T. Malkow, G. Papakonstantinou, G. Tsotridis, ... and A. A. Franco, *J. Power Sources* **304**, 207–233 (2016)
- Y. Yu, H. Li, H. Wang, X.Z. Yuan, G. Wang, M. Pan, *J. Power Sources* **205**, 10–23 (2012)
- J. Healy, C. Hayden, T. Xie, K. Olson, R. Waldo, M. Brundage, H. Gasteiger, J. Abbott, *Fuel Cells* **5**, 302–308 (2005)
- X.-Z. Yuan, Z. Shengsheng, W. Haijiang, W. Jinfeng, J.C. Sun, R. Hiesgen, K.A. Friedrich, M. Schulze, A. Haug, *J. Power Sources* **195**, 7594–7599 (2010)
- X. Huang, R. Solasi, Y.U.E. Zou, M. Feshler, K. Reifsnider, D. Condit, S. Burlatsky, T. Madden, *J. Polym. Sci. B Polym. Phys.* **44**, 2346–2357 (2006)
- P. Ferreira, Y. Shao-Horn, D. Morgan, R. Makharia, S. Kocha, H. Gasteiger, *J. Electrochem. Soc.* **152**, A2256–A2271 (2005)
- L. Gubler, S.M. Dockheer, W.H. Koppenol, *J. Electrochem. Soc.* **158**, B755–B769 (2011)
- M. Ghelichi, P.E.A. Melchy, M.H. Eikerling, *J. Phys. Chem. B* **118**, 11375–11386 (2014)
- A. Pozio, R.F. Silva, M. De Francesco, L. Giorgi, *Electrochim. Acta* **48**, 1543–1549 (2003)
- V.O. Mittal, H.R. Kunz, J.M. Fenton, *J. Electrochem. Soc.* **154**, B652–B656 (2007)
- W. Liu, D. Zuckerbrod, *J. Electrochem. Soc.* **152**, A1165–A1170 (2005)
- L. Ghassemzadeh, K.-D. Kreuer, J. Maier, K. Muller, *J. Phys. Chem. C* **114**, 14635–14645 (2010)
- M. Aoki, H. Uchida, M. Watanabe, *Electrochem. Commun.* **7**, 1434–1438 (2005)
- M. Aoki, H. Uchida, M. Watanabe, *Electrochem. Commun.* **8**, 1509–1513 (2006)
- A. Ohma, S. Suga, S. Yamamoto, K. Shinohara, *J. Electrochem. Soc.* **154**, B757–B760 (2007)
- D. Zhao, B. Yi, H. Zhang, M. Liu, *J. Power Sources* **195**, 4606–4612 (2010)
- N. Hasegawa, T. Asano, T. Hatanaka, M. Kawasumi, Y. Morimoto, *ECS Trans.* **16**, 1713–1716 (2008)
- S. Helmly, B. Ohnmacht, R. Hiesgen, E. Gülzow, K.A. Friedrich, *ECS Trans.* **58**, 969–990 (2013)
- N. Macauley, L. Ghassemzadeh, C. Lim, M. Watson, J. Kolodziej, M. Lauritzen, S. Holdcroft, E. Kjeang, *ECS Electrochem. Lett.* **2**, F33–F35 (2013)
- N. Macauley, A.S. Alavijeh, M. Watson, J. Kolodziej, M. Lauritzen, S. Knights, G. Wang, E. Kjeang, *J. Electrochem. Soc.* **162**, F98–F107 (2015)
- M.P. Rodgers, B.P. Pearman, L.J. Bonville, D.A. Cullen, N. Mohajeri, D.K. Slattery, *J. Electrochem. Soc.* **160**, F1123–F1128 (2013)
- N. Macauley, K.H. Wong, M. Watson, E. Kjeang, *J. Power Sources* **299**, 139–148 (2015)
- S. Kundu, M. Cimenti, S. Lee, D. Bessarabov, *Membrane Tech.* **10**, 7–10 (2009)
- W. Bi, G.E. Gray, T.F. Fuller, *Electrochem. Solid-State Lett.* **10**, B101–B104 (2007)
- S. Helmly, R. Hiesgen, T. Morawietz, X.-Z. Yuan, H. Wang, K.A. Friedrich, *J. Electrochem. Soc.* **160**, F687–F697 (2013)
- S. Helmly, B. Ohnmacht, P. Gazdzicki, R. Hiesgen, E. Gülzow, K.A. Friedrich, *J. Electrochem. Soc.* **161**, F1416–F1426 (2014)
- M.J. Eslamibidgoli, P.E.A. Melchy, M.H. Eikerling, *Phys. Chem. Chem. Phys.* **17**, 9802–9811 (2015)
- M.J. Eslamibidgoli, M.H. Eikerling, *ACS Catal.* **5**, 6090–6098 (2015)
- A.M. Gómez-Marín, R. Rizo, J.M. Feliu, *Catalysis Science & Technology* **4**, 1685–1698 (2014)
- N.M. Marković, H.A. Gasteiger, P.N. Ross, *J. Phys. Chem.* **99**, 3411–3415 (1995)
- N.M. Marković, H. Gasteiger, P.N. Ross, *J. Electrochem. Soc.* **144**, 1591–1597 (1997)
- A.M. Gómez-Marín, K.J.P. Schouten, M.T.M. Koper, J.M. Feliu, *Electrochem. Commun.* **22**, 153–156 (2012)
- A. Kuzume, E. Herrero, J.M. Feliu, *J. Electroanal. Chem.* **599**, 333–343 (2007)
- U.A. Paulus, A. Wokaun, G.G. Scherer, T.J. Schmidt, V. Stamenkovic, N.M. Markovic, P.N. Ross, *Electrochim. Acta* **47**, 3787–3798 (2002)
- S. Takaichi, H. Uchida, M. Watanabe, *Electrochem. Commun.* **9**, 1975–1979 (2007)
- M. Ohishi, Y. Okano, Y. Ono, A. Ohma, K. Fushinobu, K. Okazaki, *Int. J. Heat Mass Transf.* **55**, 7213–7217 (2012)
- E. Gülzow, M. Schulze, N. Wagner, T. Kaz, R. Reissner, G. Steinhilber, A. Schneider, *J. Power Sources* **86**, 352 (2000)
- E. Endoh, S. Hommura, S. Terazono, H. Widjaja, J. Anzai, *ECS Trans.* **11**, 1083–1091 (2007)